NJC

PAPER

Cite this: *New J. Chem.*, 2018, **42**, 5514

Solid-state tunable photoluminescence in gadolinium-organic frameworks: effects of the Eu^{3+} content and co-doping with Tb^{3+}†

Jarley Fagner Silva do Nascimento,[ab] Antonio Marcos Urbano de Araújo,[c] Joanna Kulesza,[d] Arthur Felipe de Farias Monteiro,[d] Severino Alves Júnior[d] and Bráulio Silva Barros *[ae]

Mixed lanthanide-organic frameworks (MLOFs) are an interesting class of hybrid materials with unique luminescence properties. The detailed structure–property relationship studies are still insufficient and therefore, the precise design and synthesis of these materials are still required. With this view, MLOFs based on Gd^{3+}, Eu^{3+} and Tb^{3+} ions and terephthalate were synthesized under solvothermal conditions, and the influence of the Eu^{3+} dopant concentration on the photophysical properties of Gd/Eu-1,4-BDC-MOFs was studied. Moreover, the effect of the excitation wavelength on color tuning in a Gd/Tb/Eu-1,4-BDC-MOF co-doped sample is also discussed here. Analyses of X-ray diffraction data indicated the Gd/Eu-1,4-BDC single phase formation in samples doped up to 7 mol% of Eu^{3+} ions. By increasing the europium content, a second crystalline phase was formed. Both crystalline phases with a metal–organic structure exhibited a red luminescence due to the characteristic 4f–4f transitions of Eu^{3+} ions. Although not observed in the X-ray diffraction patterns, most probably the second phase was also present in the sample with 7 mol% of Eu^{3+} ions, based on the results of photoluminescence. The Gd/Eu/Tb-1,4-BDC co-doped sample with 2.5 mol% of Eu^{3+} and 2.5 mol% of Tb^{3+} obtained as a single phase exhibited both red and green emissions due to the presence of Eu^{3+} and Tb^{3+} ions, respectively. Furthermore, the spectroscopic analysis indicated the energy transfer from Tb^{3+} to Eu^{3+}, which allows the color tuning by changing the excitation wavelength.

Received 26th November 2017,
Accepted 22nd February 2018

DOI: 10.1039/c7nj04625a

rsc.li/njc

Introduction

Metal–organic frameworks (MOFs) have emerged as an important class of hybrid porous materials containing metal clusters linked by organic multidentate ligands.[1] Due to their high crystallinity, chemical stability and versatility of structures and topologies,[2,3] MOFs have received considerable attention in the past two decades due to their applications in magnetism,[4] gas adsorption and separation,[5] drug delivery,[6] catalysis,[7] *etc.*

Owing to the unique luminescence properties of lanthanide ions and inherent porosity of MOFs, lanthanide-organic frameworks (LOFs) have been revealed as promising candidates for light-emitting materials,[8] sensors,[9–11] multimodal image contrast agents[12] catalysts[13] and luminescent markers for gunshot residues.[14]

Recently, considerable attention has been paid to investigate the structure–photoluminescence relationship of LOFs. However, the precise design and prediction are challenging, because of the lability of lanthanide ions combined with the lack of preferential coordination geometry.[15] Therefore, systematic and profound studies on the photophysical properties of LOFs are still required.

Regarding the diversity and flexibility of their coordination modes, aromatic polycarboxylate ligands are suitable for constructing lanthanide-organic frameworks.[16] Linear organic molecules such as terephthalic acid (1,4-H_2BDC) are attractive organic binders since they promote homogeneous network growth and some LOFs based on this ligand have already been reported.[17–21] Organic linkers not only dictate the structure of the network but also act as efficient sensitizers for lanthanide ions.

[a] *Universidade Federal do Rio Grande do Norte, Instituto de Química, 59078-970, Natal/RN, Brazil*
[b] *Instituto Federal de Educação, Ciência e Tecnologia Rio Grande do Norte, 59500-000, Macau/RN, Brazil*
[c] *Universidade Federal do Rio Grande do Norte, Escola de Ciências & Tecnologia, 59078-970, Recife/PE, Brazil*
[d] *Universidade Federal de Pernambuco, Departamento de Química Fundamental, 50070-901, Recife/PE, Brazil*
[e] *Universidade Federal de Pernambuco, Departamento de Engenharia Mecânica, Av. Prof. Moraes Rego-1235 – Cidade Universitária, 50070-901, Recife/PE, Brazil. E-mail: braulio.barros@ufpe.br*

† Electronic supplementary information (ESI) available. See DOI: 10.1039/c7nj04625a

Recently, our group has reported a new luminescent Gd-1,4-BDC-MOF doped with Eu^{3+} and demonstrated that the terephthalate ligand could act as a good sensitizer for Eu^{3+} ions due to the paramagnetic effect caused by the presence of Gd^{3+} in the matrix.[22]

As a continuation of our previous study, this paper presents a series of mixed-lanthanide-MOFs based on terephthalate. This study focused on the influence of the Eu^{3+} dopant concentration on the photophysical properties of Gd/Eu-1,4-BDC-MOFs. The effect of the excitation wavelength on color tuning in the Gd/Tb/Eu-1,4-BDC-MOF co-doped sample is also discussed here.

Experimental section

Materials

All reagents and solvents were used as received without further purification. Terephthalic acid (1,4-H_2BDC), gadolinium oxide (Gd_2O_3), europium oxide (Eu_2O_3) and terbium oxide (Tb_4O_7) were purchased from Sigma Aldrich. *N*,*N*-Dimethylformamide (DMF), ethanol (EtOH), hydrogen peroxide (H_2O_2) and nitric acid (HNO_3, 65%) were acquired from Vetec.

Synthesis of Eu-doped Gd-1,4-BDC-MOFs

To synthesize the sample doped with 1 mol% of Eu^{3+} (MLOF_Eu1%), the stoichiometric amounts of Gd_2O_3 and Eu_2O_3, 0.198 and 0.002 mmol, respectively, were dissolved in an aqueous solution of HNO_3 and kept under constant stirring at 70 °C until complete solvent evaporation. The resulting nitrates were dissolved together with 1.6 mmol of 1,4-H_2BDC in 10 mL of DMF and stirred for five minutes. Then, the solution was transferred to a Teflon-lined steel reactor and heated in an oven at 180 °C for five days. Subsequently, the mixture was cooled down to room temperature, and the obtained white solid was collected by centrifugation, washed three times with DMF and EtOH and dried at 60 °C for 24 hours.

The samples doped with 3 (MLOF_Eu3%), 5 (MLOF_Eu5%), 7 (MLOF_Eu7%) and 9 mol% of Eu^{3+} (MLOF_Eu9%) were prepared following the same procedure, however within different stoichiometric amounts of Gd_2O_3 and Eu_2O_3; 0.194 and 0.006, 0.190 and 0.010, 0.186 and 0.014, 0.182 and 0.018, respectively. For comparison, an undoped sample Gd-1,4-BDC was also prepared according to the similar synthetic procedure.

Synthesis of Eu/Tb-co-doped Gd-1,4-BDC-MOF

The co-doped Gd-1,4-BDC-MOF with 2.5 mol% of Eu^{3+} and 2.5 mol% of Tb^{3+} (MLOF_EuTb) was prepared based on the synthetic procedure described above using the following stoichiometric amounts of Gd_2O_3, Eu_2O_3, and Tb_4O_7; 0.190, 0.005 and 0.005, respectively. Hydrogen peroxide was used to reduce Tb^{4+} to Tb^{3+}.

Characterization

Powder X-ray diffraction (PXRD) analyses were conducted on a Bruker D2 Phaser diffractometer using Cu Kα radiation (λ = 1.5406 Å) with a Ni filter, operating at 30 kV and 10 mA. The PXRD patterns were recorded between 5 and 60° at steps of 0.02°. Simulated XRD patterns were obtained using the Mercury CSD 3.9 program. Thermogravimetric analyses (TGA) were performed on a Shimadzu DTG-60H thermal analysis system. The samples were heated from 30 °C to 900 °C at a rate of 10 °C min^{-1} under a nitrogen atmosphere. Attenuated total reflection Fourier transform infrared (ATR-FTIR) experiments were carried out using a Bruker Vertex 70/v spectrometer. Morphological analysis of powders was performed by Scanning Electron Microscopy (SEM) using an FEI Quanta 200 FEG microscope. The excitation and emission spectra were recorded in the solid state at 298 K using a Fluorolog3 Horiba Jobin Yvon spectrofluorometer equipped with Hamamatsu R928P photomultiplier, SPEX 1934 D phosphorimeter, and a pulsed 150 W Xe–Hg lamp.

Results and discussion

The synthesized samples were characterized by powder X-ray diffraction (PXRD) to identify the obtained crystalline phases. The corresponding experimental and simulated diffractograms are shown in Fig. 1.

As can be seen, the samples doped up to 7 mol% of Eu^{3+} as well as the sample codoped with Tb^{3+} present a single-phase, whereas in the PXRD pattern of the sample doped with 9 mol% of Eu^{3+} ions two phases are observed. These phases are isostructural with $[Eu_2(BDC)_3(DMF)_2(H_2O)\cdot DMF]$ and $[Eu_2(BDC)_3(DMF)_2(H_2O)_2]$, here named MLOF1 and MLOF2, respectively. However, one can note the discrepancy of intensity between the diffraction peaks at about 9.4 and 9.7° in the MLOF1 phase in the experimental and simulated patterns. The crystal structure of MLOF1 was previously reported by Decadt and coworkers[23] and most recently by our group.[22]

It consists of a 3D structure with porous channels along the crystallographic direction "[111]". These channels are formed by 1D chains cross-linked to each other by 1,4-BDC^{2-} ligands. Fig. 2a exhibits the 3D channels of MLOF1 without any DMF molecules for better clarity. There are two different types of

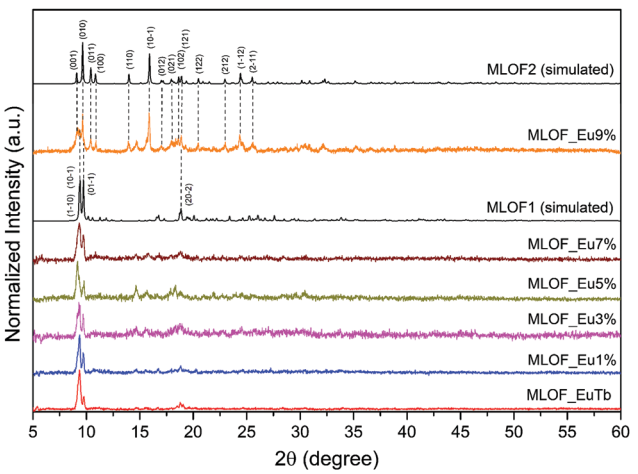

Fig. 1 X-ray powder diffraction pattern of the synthesized MLOF samples in comparison with the simulated from single crystal data PXRD patterns of MLOF1 and MLOF2.

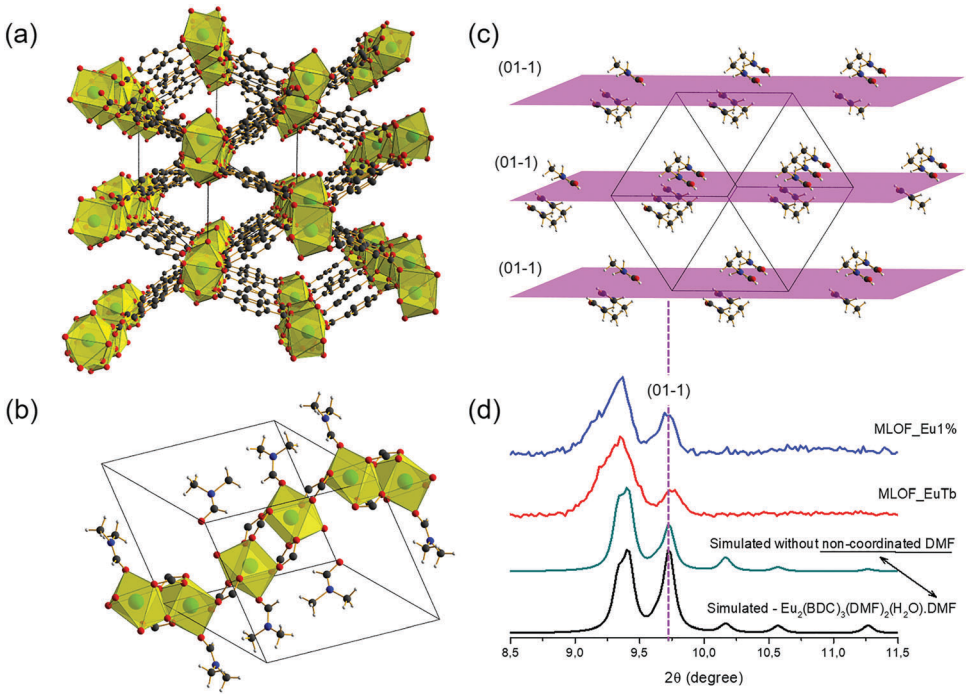

Fig. 2 (a) Projection along the *c* axis of the partially expanded net structure and (b) the coordination environment of the Eu^{3+} dimer in the crystal structure of MLOF1 with both coordinated and non-coordinated DMF molecules. (c) View of the lattice plane (01−1) displaying non-coordinated DMF molecules and (d) simulated PXRD pattern of MLOF1 without non-coordinated DMF molecules. Color code: black (carbon), red (oxygen), blue (nitrogen), grey (hydrogen) and green (gadolinium or europium). Polyhedra in yellow represent lanthanide sites.

binuclear inorganic building blocks in the chains, where lanthanide ions are surrounded by oxygen atoms from the 1,4-BDC^{2-}, DMF and water molecules. Additional guest DMF molecules are found in the porous channels (non-coordinated DMF). The two kinds of building blocks together with the coordinated and non-coordinated DMF molecules present in the structure are depicted in Fig. 2b. It was observed that the non-coordinated DMF molecules are distributed through the lattice plane (01−1), contributing to the diffraction peak intensity with the same Miller indices at 9.7° (Fig. 2c). This peak appears less intense in the experimental patterns compared to the simulated pattern for $[Eu_2(BDC)_3(DMF)_2(H_2O)\cdot DMF]$. Therefore, another simulated diffraction pattern was calculated without considering the presence of non-coordinated DMF molecules. Fig. 2d exhibits both, simulated and experimental patterns of the MLOF_Eu1% and MLOF_EuTb samples. It can be clearly seen that without non-coordinated DMF, the intensity of the diffraction peak at 9.7° decreases compared to the peak at 9.4°, which suggests the absence of the guest DMF molecules in the channels of the crystal lattice. The peak at 9.4° corresponds to the overlapping of the diffraction peaks related to the lattice planes (1−10) and (10−1), at 9.33 and 9.41°, respectively (Fig. 2d). We assume that the left shoulder of the peak at 9.4° observed in the experimental patterns corresponds to the peak shift related to the lattice plans (1−10) indicating a slight deformation in the unit cell. Such deformation may be attributed to the slight difference in the cation radius[23] of the lanthanide ions Gd and Eu, both present in the prepared samples; whereas the simulated data were calculated for a Eu-based MOF.

Also, the phenomenon known as breathing may provoke a change in the unit cell volume upon external stimuli (*e.g.*, guest molecule adsorption/desorption).[24] Such a phenomenon has been observed in several MOFs, such as in the MIL-53(M) family ($[M(bdc)(OH)]_n$ with bdc = 1,4-benzenedicarboxylate, and M = Al, Fe, Cr, Sc, Ga, In).[24–31]

The crystal structure of MLOF2 was previously described by Zhang and coworkers.[32] There is just one binuclear inorganic building block coordinated by two water and two DMF molecules. The building blocks are connected to each other by six 1,4-BDC^{2-} molecules (see Fig. S1a, ESI†), providing a 3D structure with porous channels along the crystallographic *b* axis. Fig. S1b (ESI†) exhibits the 3D channels without any DMF or water molecules for better clarity.

Thermal analyses (TGA-DrTGA) have confirmed the absence of guest DMF in the lattice channels, as can be seen in Fig. S2 (ESI†). Except for the MLOF_Eu9% sample, only one lower-temperature mass-loss event was observed from 90 to 220 °C, related to the coordinated solvent molecules (DMF and water). In the case of non-coordinated DMF molecules present in the structure, the second lower temperature mass-loss event could be observed. The synthesized MOFs are thermally stable until 450 °C, at which temperature the organic ligand begins to decompose, and the lattice collapses. The MLOF_Eu9% sample exhibits the first mass-loss stage longer than for other samples, until 300 °C, probably due to the presence of the secondary phase.

FTIR spectra of the samples containing different Eu^{3+} dopant concentrations and of the terephthalic acid are presented in Fig. 3. The absence of the band at around 1670 cm^{-1}

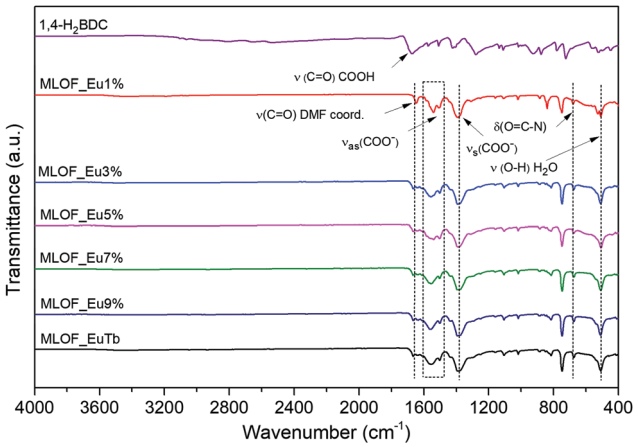

Fig. 3 Absorption spectra in the infrared region for 1,4-H_2BDC and MLOF samples.

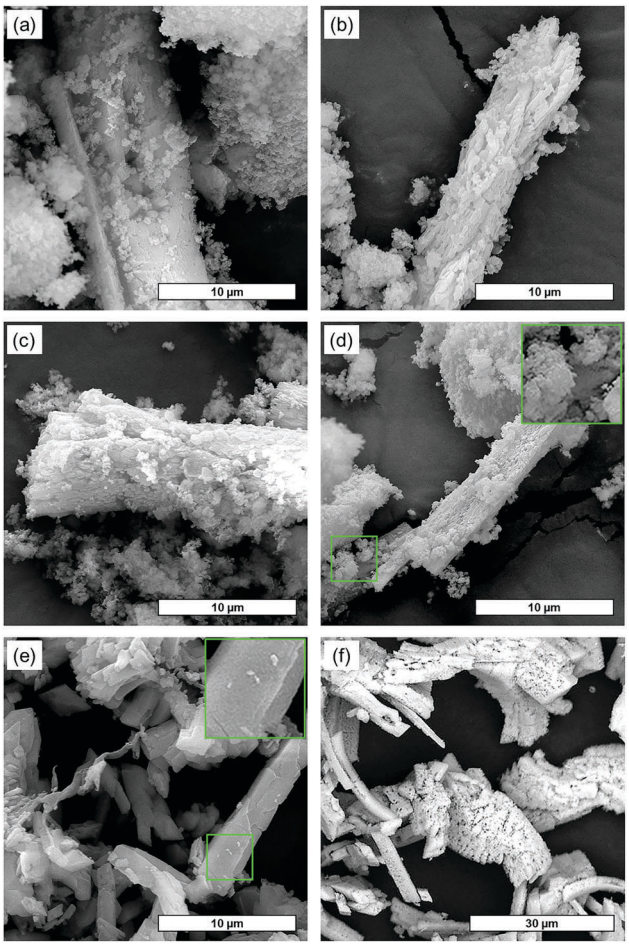

Fig. 4 SEM images of powder MLOF samples: (a) MLOF_Eu1%, (b) MLOF_Eu3%, (c) MLOF_Eu5%, (d) MLOF_Eu7%, (e) MLOF_Eu9%, and (f) MLOF_EuTb.

corresponding to the stretching vibration of the C═O bond in COOH confirms that all carboxylate groups in the MLOF samples are coordinated to the metal center. All spectra are very similar to each other. The bands in the region between 1555 and 1501 cm^{-1} and at 1384 cm^{-1} attributed, respectively, to the stretching, asymmetric (ν_{as}) and symmetric (ν_s) vibrations of the COO^- groups, can be observed for all samples. The difference between (ν_{as}) and (ν_s), equal to $\Delta\nu$ = 171 and 117 cm^{-1} might indicate the bidentate bridging and tridentate bridging-chelating coordination modes of carboxylates,[33] which are in agreement with the analysis of the crystal structure of the samples. The MLOF_Eu9% sample, which is a mixture of phases, presents a very similar IR spectrum compared to the pure-phase samples, as a result of the similarity of the existing coordination modes. Therefore, no additional bands are observed in the IR spectrum, or the bands corresponding to both phases are superimposed in the same region.

The IR spectra show the presence of coordinated solvent molecules, which are in line with the description of the crystal structures. The bands around 1647–1662 cm^{-1} and at 676 cm^{-1} may be attributed to the stretching ν(C═O) and bending δ(OCN) vibrations of the coordinated DMF molecule.[34] The FTIR spectra of all samples also present bands at 3427 and 510 cm^{-1}, suggesting the presence of coordinated water molecules.

Morphological analysis of the synthesized samples was conducted by scanning electron microscopy (SEM), and the micrographs are shown in Fig. 4. The powders of MLOF_Eu1%–MLOF_Eu7% and MLOF_EuTb show the same morphology (see Fig. 4a–d and f).

The powders are composed of submicrometer primary particles, which in some cases assemble into soft micrometric agglomerates. As expected, the increase in the dopant content did not cause significant changes in the way the particles clustered. However, when the dopant concentration reaches 9% in mol and a second phase crystallizes, the morphology changes from soft (porous clusters of particles) to hard (non-porous) agglomerates highlighted in green frames in Fig. 4d and e, respectively. However, this change in morphology seems to be related to the crystalline structure of the second phase and not to the dopant concentration.

The excitation spectra of MLOFs were obtained by monitoring the emission of the $^5D_0 \rightarrow {}^7F_2$ transition of the Eu^{3+} ions at 614–615 nm (Fig. 5).

The broadband at the range of 250–350 nm and two relatively low-intensity $^7F_0 \rightarrow {}^5D_4$, $^5L_6$ transitions of the Eu^{3+} ions at 362 and 394 nm, respectively, can be seen. Because the 4f sublevels of Gd^{3+} ions are located above the triplet levels of most organic linkers, the emissions of these metal centers cannot be observed. The broadband has two components with maxima at 298 and 325 nm, probably, assigned to the organic ligand (1,4-BDC) excited states. These two bands are slightly shifted compared to the pure terephthalic acid (1,4-H_2BDC) bands as a consequence of the coordination of the metal center to the ligand (see Fig. S3, ESI†). However, the contribution of ligand-to-metal charge transfer (LMCT) cannot be entirely excluded.[35–37]

Fig. 6a–d show the emission spectra and the decay curves of MLOFs. The spectra are composed of sharp emission lines assigned to the $^5D_0 \rightarrow {}^7F_{0,1,2,3,4}$ transitions from Eu^{3+} ions.[14] The presence of the $^5D_0 \rightarrow {}^7F_0$ transition at 578 nm indicates that the Eu^{3+} ions are embedded in a low symmetry environment

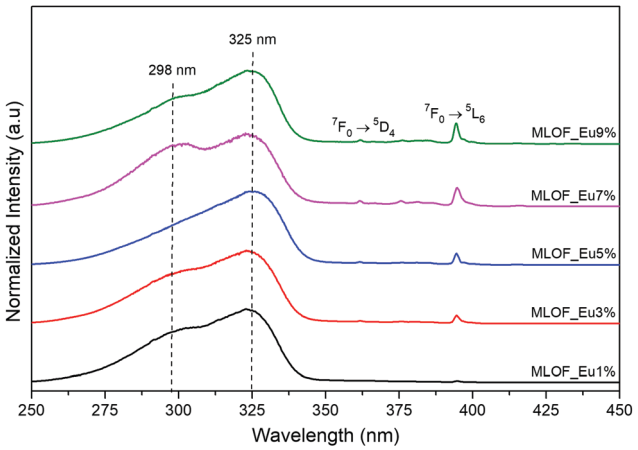

Fig. 5 Excitation spectra of MLOF_Eu1%–MLOF_Eu9% samples measured at room temperature by monitoring the Eu^{3+} emission at 614 nm.

without an inversion center, typically C_{nv}, C_n or C_s.[9] The careful analysis of the splitting of each Eu^{3+} transition may suggest that the Eu^{3+} in pure-phase MLOF_Eu1%–MLOF_Eu7% samples is embedded in the approximate C_{4v} symmetry-site, according to the diagram elaborated by Sengupta *et al.*[38] Moreover, the $^5D_0 \rightarrow {}^7F_2$ electric dipole transition, which is sensitive to the first coordination sphere, has a higher intensity than the $^5D_0 \rightarrow {}^7F_1$ magnetic dipole transition, confirming that Eu^{3+} ions occupy a low symmetry site and without an inversion center.[39,40]

Upon direct excitation of the $^5L_6$ energy level of the Eu^{3+} ions (394 nm), the MLOF_Eu9% sample presents different emission profiles in comparison to that of other MLOF samples. These changes, especially visible for the $^5D_0 \rightarrow {}^7F_2$ transition, are due to the presence of two distinct crystalline phases; the secondary phase certainly possesses different crystalline fields around the Eu^{3+} site which causes splitting of the emission band (see Fig. 6a). Also, the decay curve obtained by monitoring the emission at 614 nm (see Fig. 6b) does not match with curves obtained for the other samples. Although less visible, the curve obtained for the MLOF_Eu7% sample depicted a similar behavior, which may indicate the presence of the MLOF2 crystalline phase. The MLOFs showed very similar emission spectra and decay curve profiles when excited at 325 nm (see Fig. 6c and d). However, the relative intensity of the emission lines depends on the Eu^{3+} ion concentration, which is also observed in Fig. 6a. The curve of the MLOF_Eu9% sample fitted well with a bi-exponential function as expected for the sample presenting two phases. Although MLOF_Eu1% to MLOF_Eu7% samples present two slightly different sites, all decay curves were found to fit a mono-exponential function, as a consequence of closely related time-dependent photoluminescence behavior of both sites, as also observed in our previous studies.[22]

The emission lifetimes are summarized in Table 1. It seems that the lifetime values are almost independent of the Eu^{3+} ion concentrations up to 7%, increasing substantially only for the sample with the highest content of Eu^{3+} (9%). We also note that upon excitation at 394 nm, the average lifetime value is higher than the one observed upon excitation at 325 nm, which is expected since the MLOF2 phase is not sensitive to the excitation at 325 nm.

Fig. 7 shows the emission spectra recorded upon excitation at 280, 300, 325 and 394 nm and the excitation spectra obtained by monitoring the MLOF_Eu9% sample at 614 and 618 nm. While the emission spectrum obtained upon excitation at 325 nm presents only one $^7F_2$ Stark level, the spectra recorded upon excitation at 280, 300 and 394 nm show the splitting of

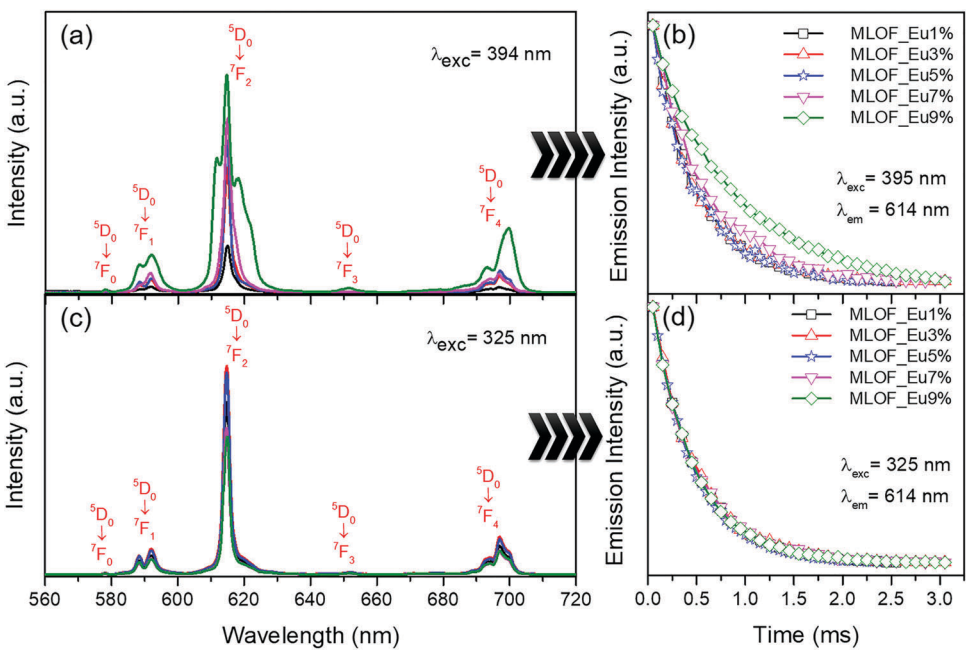

Fig. 6 Emission spectra of the MLOF_Eu1%–MLOF_Eu9% samples acquired at room temperature upon excitation at (a) 395 nm and (c) 325 nm. Decay emission curves obtained at 298 K upon excitation of the MLOF_Eu1%–MLOF_Eu9% samples at (b) 394 nm and (d) 325 nm.

Table 1 Lifetime for the samples MLOF_Eu1%, MLOF_Eu3%, MLOF_Eu5%, MLOF_Eu7% and MLOF_Eu9%

Sample	λ_{exc} (nm)	λ_{em} (nm)	τ (ms)	τ_1	τ_2	τ_{av} (ms)
MLOF_Eu1%	394	614	0.30	—	—	—
MLOF_Eu3%	394	614	0.30	—	—	—
MLOF_Eu5%	394	614	0.31	—	—	—
MLOF_Eu7%	394	614	0.32	—	—	—
MLOF_Eu9%	394	614	—	0.65	0.11	0.568
	394	618	—	0.647	0.109	0.572
MLOF_Eu1%	325	614	0.30	—	—	—
MLOF_Eu3%	325	614	0.31	—	—	—
MLOF_Eu5%	325	614	0.30	—	—	—
MLOF_Eu7%	325	614	0.31	—	—	—
MLOF_Eu9%	325	614	—	0.43	0.27	0.47

the $^5D_0 \rightarrow {}^7F_2$ transition in four Stark components (see Fig. 7a and b). It is worth noting that the spectra collected upon excitation at 325 nm are similar to those obtained for the samples with a lower concentration of Eu^{3+} ions, which present a single crystalline phase (MLOF1). Thus, the Stark components observed at about 611, 614, 618 and 622 nm seem to be a consequence of the selective excitation of the second crystalline phase (MLOF2).

In the case of the structure MLOF1, the Eu^{3+} ions are coordinated by eight oxygen atoms in a distorted square antiprism geometry with C_{4v} or C_4 symmetry, while in the structure of MLOF2, the ions are coordinated by nine oxygen atoms in a distorted monocapped square antiprism geometry with C_{2v} symmetry or lower.[41] Both coordination spheres are depicted in Fig. 7a.

According to Binnemans,[42] the crystal-field perturbation destroys the spherical symmetry of the free-ion and the $^{2S+1}L_J$ terms split up in a number of crystal-field levels. The $2J + 1$ degeneracy of a $^{2S+1}L_J$ term may be, to some extent, removed depending on the symmetry class or, in other words, the number of split terms depends on the coordination environment. This can explain why the MLOF1 and MLOF2 phases show such different emission spectra, most specifically regarding the $^5D_0 \rightarrow {}^7F_2$ transition, which is hypersensitive to the coordination environment. The emission spectra from the MLOF1 phase does not match well with the spectrum reported by Decadt and co-workers,[23] surprisingly it resembles the one attributed to the MLOF2 phase.

However, the emission spectra corresponding to the phase designated here as MLOF1 are very similar to those reported by Mustafa *et al.*[43] and Wang *et al.*,[44] in both cases obtained from crystalline phases where the Eu^{3+} ions are embedded in sites with a distorted square antiprism geometry and coordination number eight. On the other hand, the higher number of split terms in the case of the phase designated here as MLOF2 was also observed by Kang and co-workers,[45] in an Eu(III) complex with nitrilotriacetate, where the trivalent europium ions are embedded in sites with a distorted capped square antiprism geometry and coordination number nine.

Fig. 7c shows the excitation spectra obtained by monitoring the emissions at 614 and 618 nm, respectively. In both cases, two broad bands are observed with maxima at 298 and 325 nm, respectively, as well as the $^7F_0 \rightarrow {}^5L_6$ transition of Eu^{3+} ions at 394 nm. We assume that the excitation broadband at 325 nm, which appears to be sensitive to the monitoring wavelength, belongs to the MLOF1 phase; whereas the excitation broadband at 298 nm is related to both MLOF1 and MLOF2 phases.

Tunable luminescence properties may be conferred to hybrid host matrices by co-doping with different lanthanide ions and controlled by the excitation wavelength. Fig. 8 shows

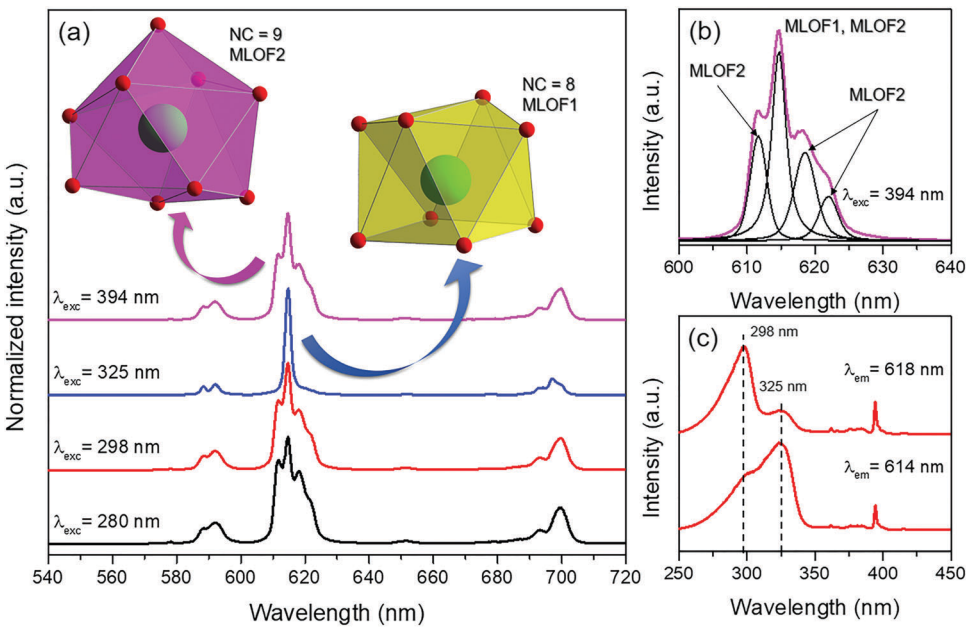

Fig. 7 (a and b) Emission spectra of the MLOF_Eu9% sample recorded at room temperature upon excitation at 280, 298, 325 and 394 nm and (c) excitation spectra of the MLOF_Eu9% sample obtained by monitoring the emission at 614 and 618 nm.

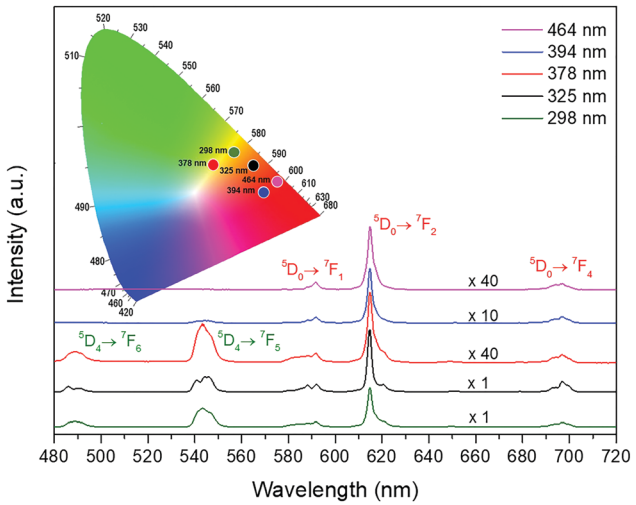

Fig. 8 Emission spectra of MLOF_EuTb acquired at room temperature upon excitation at 265, 300, 323, 378, 395 and 464 nm and CIE diagram points of MLOF_EuTb for different excitation wavelengths.

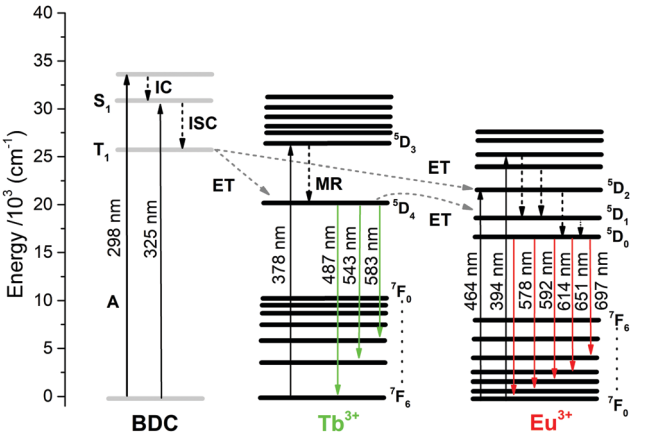

Fig. 9 Schematic representation of photophysical processes in doped samples (antenna effect). A = absorption, S_1 = singlet state, IC = internal conversion, ISC = intersystem crossing, T_1 = triplet state, and ET = transfer energy.

the emission spectra of the Eu^{3+}/Tb^{3+} co-doped sample (MLOF_EuTb) obtained under different excitation wavelengths. The spectra obtained under organic ligand excitation at 298 and 325 nm are much more intense than those obtained *via* direct excitation of the lanthanide ions at 378, 394 and 464 nm. Again, the antenna effect is the most efficient energy transfer mechanism.

By exciting of the $^5L_6$ and $^5D_2$ energy levels of Eu^{3+} ions at 394 and 464 nm, respectively, only the $^5D_0 \rightarrow {}^7F_J$ transitions of the Eu^{3+} ions are observed confirming no energy transfer from Eu^{3+} to Tb^{3+} ions. On the other hand, by exciting the $^5G_6$, $^5D_3$ energy levels of Tb^{3+} ions at 378 nm both, Tb^{3+} ($^5D_4 \rightarrow {}^7F_J$) and Eu^{3+} ($^5D_0 \rightarrow {}^7F_J$) transitions are observed. In this case, the energy transfer from Tb^{3+} to Eu^{3+} ions may be confirmed.

The chromatic coordinates (CIE 1931 and field of view 2 degrees) were calculated using the SPECTRA LUX[46] program and are shown in Fig. 8. It is observed that the color of the emission can be tuned from green to red passing through the orange color in the function of the excitation wavelength.

Fig. 9 shows the schematic representation of the most probable energy transfer mechanisms in the MLOFs. These mechanisms were proposed based on the studies of Crosby and Whan.[47–49]

The excitation process may occur from the ground state (S_0) to the first excited singlet state (S_1) of the BDC ligand *via* absorption (A) at 298 e 325 nm. In the first case, the absorption is followed by an internal conversion (IC) from the higher to the lower vibrational energy levels of S_1 and an exchange of multiplicity for the triplet state (T_1) originating from the intersystem crossings (ISC).

The energy transfer from T_1 to the excited states of the lanthanides may proceed by two different ways. In the first case, the energy is transferred to the Eu^{3+} excited $^5D_2$ state resonant with the linker triplet level. As a rule, the energy gap between the triplet state and the emitting level should be between 1500 and 5000 cm^{-1} to observe efficient luminescence of the Eu^{3+}.[42] Posteriorly, non-radiative relaxation occurs, followed by radiative decays from the $^5D_0$ (Eu^{3+}) level to $^7F_{0-4}$. In the second case, we have the energy transfer to the $^5D_4$ excited state of Tb^{3+}. Then, the photon returns to the ground state generating the terbium emissions ($^5D_4 \rightarrow {}^7F_{6,5,4}$) or transfers this energy to the excited $^5D_1$ energy level of Eu^{3+} followed by the relaxation to the emissive $^5D_0$ level.

The mechanisms related to the direct excitation of the Tb^{3+} (λ_{exc} = 378 nm) and Eu^{3+} (λ_{exc} = 394 and 464 nm) ions can be described as follows. The direct excitation process of Tb^{3+} ions occurs from the absorption of ultraviolet radiation (λ = 378 nm) promoting the photon transfer from the ground state $^7F_6$ to the excited state $^5D_3$, which posteriorly decays *via* multiphonon relaxation (MR) to the $^5D_4$ emitting level. From the $^5D_4$ level, the photon decay originating the characteristic $^5D_4 \rightarrow {}^7F_{6,5,4}$ emissions or transfer its energy to the excited levels of lower energy ($^5D_0$) of the Eu^{3+} ions.[39]

The direct excitation of Eu^{3+} ions in MLOFs may occur by absorption of ultraviolet radiation (λ = 394 or 464 nm) promoting the photons from the $^7F_0$ ground state to the $^5D_4$ and $^5D_2$ excited states, respectively. Subsequently, both decay non-radiatively to the emitter $^5D_0$ level and then generate the characteristic $^5D_0 \rightarrow {}^7F_{0-4}$ emissions of Eu^{3+} ions.

Conclusions

Mixed lanthanide-organic frameworks based on Gd^{3+}, Eu^{3+} and Tb^{3+} ions and terephthalate were successfully synthesized *via* a hydrothermal method and the purity of MLOF samples was dictated by the Eu^{3+} dopant concentration. The results indicated that up to 5 mol% of the trivalent lanthanide ions such as Eu and Tb may be embedded into the structure of Gd-BDC without the formation of secondary phases. Both, the primary and the secondary phases present binuclear inorganic building blocks but with different symmetry environments, which was confirmed based on the emission spectra and the decay curves. The Gd-BDC compounds doped with Eu^{3+} ions showed red luminescence, while the sample co-doped with Tb^{3+} ions demonstrated a tunable color as a function of the excitation

wavelength. For all samples, including the Eu–Tb co-doped one, the antenna effect from the organic ligand to the lanthanide ions was the most efficient excitation mechanism. In the case of the co-doped sample, the antenna effect was observed for both ions; however, the most efficient mechanism involved the energy transfer from the ligand to Tb^{3+} ions, and from Tb^{3+} to Eu^{3+} ions. No energy transfer from Eu^{3+} to Tb^{3+} ions was identified. Moreover, the multiple mechanisms of excitation and energy transfer allow the tuning of the emission color, turning this material into an attractive candidate for optical applications.

Conflicts of interest

There are no conflicts to declare.

Acknowledgements

The authors thank the Federal University of Pernambuco, School of Science and Technology/UFRN and the Federal Institute of Education, Science and Technology of the Rio Grande do Norte (IFRN). This work was supported by CNPq (grant no. 407445/2013-7) and PRONEX/FACEPE/CNPq (grant no. APQ-0675-1.06/14).

References

1 A. Corma, H. García and F. X. Llabrés i Xamena, *Chem. Rev.*, 2010, **110**, 4606–4655.
2 G. S. Papaefstathiou and L. R. MacGillivray, *Coord. Chem. Rev.*, 2003, **246**, 169–184.
3 Z. Bian and C. Huang, *Rare Earth Coordination Chemistry: Fundamentals and Applications*, John Wiley & Sons (Asia) Pte Ltd, 2010, pp. 435–472.
4 P. Dechambenoit and J. R. Long, *Chem. Soc. Rev.*, 2011, **40**, 3249–3265.
5 X.-J. Wang, P.-Z. Li, Y. Chen, Q. Zhang, H. Zhang, X. X. Chan, R. Ganguly, Y. Li, J. Jiang and Y. Zhao, *Sci. Rep.*, 2013, **3**, 1149–1153.
6 H. Ren, L. Zhang, J. An, T. Wang, L. Li, X. Si, L. He, X. Wu, C. Wang and Z. Su, *Chem. Commun.*, 2014, **50**, 1000–1002.
7 Y.-B. Huang, J. Liang, X.-S. Wang and R. Cao, *Chem. Soc. Rev.*, 2017, **46**, 126–157.
8 Y. Cui, Ch. Banglin and Q. Guodong, *Coord. Chem. Rev.*, 2014, **273**, 76–86.
9 B. Chen, L. Wang, Y. Xiao, F. R. Fronczek, M. Xue, Y. Cui and G. Qian, *Angew. Chem., Int. Ed.*, 2009, **48**, 500–503.
10 B. V. Harbuzaru, A. Corma, F. Rey, P. Atienzar, J. L. Jordá, H. García and J. Rocha, *Angew. Chem., Int. Ed.*, 2008, **47**, 1080–1083.
11 F. Pellé, P. Aschehoug, S. Surblé, F. Millange, C. Serre and G. Férey, *J. Solid State Chem.*, 2010, **183**, 795–802.
12 K. M. Taylor, A. Jin and W. Lin, *Angew. Chem.*, 2008, **120**, 7836–7839.
13 J. Lee, O. K. Farha, J. Roberts, K. A. Scheidt, S. T. Nguyen and J. T. Hupp, *Chem. Soc. Rev.*, 2009, **38**, 1450–1459.
14 I. T. Weber, A. J. G. de Melo, M. A. D. M. Lucena, M. O. Rodrigues and S. A. Júnior, *Anal. Chem.*, 2011, **83**, 4720–4723.
15 Y. Han, X. Li, L. Li, C. Ma, Z. Shen, Y. Song and X. You, Structures and properties of porous coordination polymers based on lanthanide carboxylate building units, *Inorg. Chem.*, 2010, **49**, 10781–10787.
16 F. A. A. Paz, J. Klinowski, S. M. Vilela, J. P. Tome, J. A. Cavaleiro and J. Rocha, Ligand design for functional metal–organic frameworks, *Chem. Soc. Rev.*, 2012, **41**, 1088–1110.
17 X. P. Yang, R. A. Jones, J. H. Rivers and R. P. J. Lai, *Dalton Trans.*, 2007, 3936–3942.
18 T. M. Reineke, M. Eddaoudi, M. Fehr, D. Kelley and O. M. Yaghi, *J. Am. Chem. Soc.*, 1999, **121**, 1651–1657.
19 A. Deluzet, W. Maudez, C. Daiguebonne and O. Guillou, *Cryst. Growth Des.*, 2003, **3**, 475–479.
20 L. Pan, N. Zheng, Y. Wu, S. Han, R. Yang, X. Huang and J. Li, *Inorg. Chem.*, 2001, **40**, 828–830.
21 X. Guo, G. Zhu, F. Sun, Z. Li, X. Zhao, X. Li and S. Qiu, *Inorg. Chem.*, 2006, **45**, 2581–2587.
22 J. F. S. Nascimento, B. S. Barros, J. Kulesza, J. B. L. de Oliveira, A. K. P. Leite and R. S. Oliveira, *Mater. Chem. Phys.*, 2017, **190**, 166–174.
23 R. Decadt, K. Van Hecke, D. Depla, K. Leus, D. Weinberger, I. Van Driessche and R. Van Deun, *Inorg. Chem.*, 2012, **51**, 11623–11634.
24 A. Schneemann, V. Bon, I. Schwedler, I. Senkovska, S. Kaskel and R. A. Fischer, *Chem. Soc. Rev.*, 2014, **43**, 6062–6096.
25 T. Loiseau, C. Serre, C. Huguenard, G. Fink, F. Taulelle, M. Henry, T. Bataille and G. Férey, *Chem. – Eur. J.*, 2004, **10**, 1373–1382.
26 F. Millange, N. Guillou, R. I. Walton, J. M. Grenèche, I. Margiolaki and G. Férey, *Chem. Commun.*, 2008, 4732–4734.
27 F. Millange, C. Serre and G. Férey, *Chem. Commun.*, 2002, 822–823.
28 C. Serre, F. Millange, C. Thouvenot, M. Noguès, G. Marsolier, D. Louër and G. Férey, *J. Am. Chem. Soc.*, 2002, **124**, 13519–13526.
29 J. P. Mowat, V. R. Seymour, J. M. Griffin, S. P. Thompson, A. M. Slawin, D. Fairen-Jimenez and P. A. Wright, *Dalton Trans.*, 2012, **41**, 3937–3941.
30 C. Volkringer, T. Loiseau, N. Guillou, G. Férey, E. Elkaïm and A. Vimont, *Dalton Trans.*, 2009, 2241–2249.
31 E. V. Anokhina, M. Vougo-Zanda, X. Wang and A. J. Jacobson, *J. Am. Chem. Soc.*, 2005, **127**, 15000–15001.
32 Z. H. Zhang, S. Y. Wan, T. A. Okamura, W. Y. Sun and N. Ueyama, *Z. Anorg. Allg. Chem.*, 2006, **632**, 679–683.
33 G. B. Deacon and R. J. Phillips, *Coord. Chem. Rev.*, 1980, **33**, 227–250.
34 S. Akopyan, H. Bertagnolli, I. Boyarskaya, D. Leicht, R. Merkle, L. Solovieva and E. Vilaseca, *Phys. Chem. Chem. Phys.*, 2001, **3**, 2098–2104.
35 M. D. Allendorf, C. A. Bauer, R. K. Bhakta and R. J. T. Houk, *Chem. Soc. Rev.*, 2009, **38**, 1330–1352.
36 J. Fan, H. F. Zhu, T. A. Okamura, W. Y. Sun, W. X. Tang and N. Ueyama, *New J. Chem.*, 2003, **27**, 1409–1411.
37 C. D. E. S. Barbosa, L. L. da Luz, F. A. Paz, O. L. Malta, M. O. Rodrigues, S. A. Júnior and L. D. Carlos, *RSC Adv.*, 2017, **7**, 6093–6101.

38 A. Sengupta, S. V. Godbole, P. K. Mohapatra, M. Iqbal, J. Huskens and W. Verboom, *J. Lumin.*, 2014, **148**, 174–180.
39 R. S. de Oliveira, B. S. de Brito, J. Kulesza, S. Alves, Jr. and B. S. Barros, *Ceram. Int.*, 2017, **43**, 8276–8283.
40 T. Zhu, P. Chen, H. Li, W. Sun, T. Gao and P. Yan, *Phys. Chem. Chem. Phys.*, 2015, **17**, 16136–16144.
41 C. Cascales, R. Balda, V. Jubera, J. P. Chaminade and J. Fernández, *Opt. Express*, 2008, **16**, 2653–2662.
42 K. Binnemans, *Coord. Chem. Rev.*, 2015, **295**, 1–45.
43 D. Mustafa, I. G. N. Silva, S. R. Bajpe, J. A. Martens, C. E. A. Kirschhock, E. Breynaert and H. F. Brito, *Dalton Trans.*, 2014, **43**, 13480–13484.
44 L.-F. Wang, L.-C. Kang, W.-W. Zhang, F.-M. Wang, X.-M. Ren and Q.-J. Meng, *Dalton Trans.*, 2011, **40**, 9490–9497.
45 J. G. Kang, J. P. Hong, S. K. Yoon, J. H. Bae and Y. D. Kim, *J. Alloys Compd.*, 2002, **339**, 248–254.
46 P. A. Santa-Cruz and F. S. Teles, *Spectra Lux Software v. 2.0. Ponto Quântico Nanodispositivos/RENAMI.*, 2003.
47 G. A. Crosby, R. E. Whan and J. J. Freeman, *J. Phys. Chem.*, 1962, **66**, 2493–2499.
48 R. E. Whan and G. A. Crosby, *J. Mol. Spectrosc.*, 1962, **8**, 315–327.
49 G. A. Crosby, R. E. Whan and R. M. Alire, *J. Chem. Phys.*, 1961, **34**, 743–748.

